Electronic Structure and Compton Profiles of Tungsten

Babu Lal Ahuja[a], Ashish Rathor[a], Vinit Sharma[a], Yamini Sharma[b],
Ashvin Ramniklal Jani[c], and Balkrishna Sharma[d]

[a] Department of Physics, University College of Science, M. L. Sukhadia University, Udaipur-313001,
Rajasthan, India
[b] Department of Physics, Feroze Gandhi College, Rae Bareli-229001, U.P., India
[c] Department of Physics, Sardar Patel University, Vallabh Vidyanagar-388120, Gujarat, India
[d] Department of Physics, University of Rajasthan, Jaipur-302004, Rajasthan, India

Reprint requests to Prof. B. L. A.; E-mail: blahuja@yahoo.com

The energy bands, density of states and Compton profiles of tungsten have been computed using band structure methods, namely the spin-polarized relativistic Korringa-Kohn-Rostoker (SPR-KKR) approach as well as the linear combination of atomic orbitals with Hartree-Fock scheme and density functional theory. The full potential linearized augmented plane wave scheme to calculate these properties and the Fermi surface topology (except the momentum densities) have also been used to analyze the theoretical data on the electron momentum densities. The directional Compton profiles have been measured using a 100 mCi ^{241}Am Compton spectrometer. From the comparison, the measured anisotropies are found to be in good agreement with the SPR-KKR calculations. The band structure calculations are also compared with the available data.

Key words: X-Ray Scattering; Band Structure Calculations; Fermi Surface of Metals.
PACS numbers: 13.60.Fz, 71.15.Ap, 71.15.Mb, 71.18.+y

1. Introduction

During the past few years, several authors [1 – 8] have reported on the electronic and optical properties of W using non-self-consistent, self-consistent, non-relativistic and scalar-relativistic electronic band structure calculations. The partial success of these calculations has put increasing interest in some improved electronic structure calculations. It is well known that the Compton profile, $J(p_z)$, provides a useful test of ab-initio electronic structure calculations [9, 10]. Regarding Compton scattering studies on W, isotropic Compton profiles employing 59.54 keV γ-rays have been reported [11]. The electron momentum densities and directional Compton profiles using semi-relativistic augmented plane wave (APW) calculations within the local density approximation (LDA) have also been computed [12]. In these calculations, relativistic mass-velocity corrections have been incorporated, while the spin-orbit coupling has been neglected.

The objectives of the present investigations are: (a) to calculate some electronic properties of a 5d heavy transition metal like W using different electronic structure schemes and compare it with the available data; (b) to compare the theoretical directional Compton profiles with our directional experimental findings and the available theoretical profiles; and (c) to interpret the experimental data of W in terms of Fermi surface topology.

This article presents a benchmark study on the energy bands and the density of states using a linear combination of atomic orbitals (LCAO) within the Hartree-Fock (HF) scheme and the density functional theory (DFT), full-potential linearized APW (FP-LAPW) calculations, and the spin-polarized relativistic Korringa-Kohn-Rostoker (SPR-KKR) approach. The directional Compton profiles have also been computed using the LCAO and the SPR-KKR formalisms. To compare and contrast our theoretical results, we have also measured the directional Compton profiles of W, using our first ever shortest geometry-based 100 mCi ^{241}Am (59.54 keV) Compton spectrometer.

2. Computations

2.1. KKR Calculations

Our first-principles calculations were based on the SPR-KKR within the LDA approach [13 – 15]. In this

method, the crystal potential is treated within the atomic sphere approximation. The restriction of the angular momentum expansion for the major component of the wave function to l_{max} leads to a neutral cut-off for the expansion of all other quantities relevant for the self-consistent field (SCF) iteration. In the present calculations for bcc W ($a = 3.165$ Å) a cut-off of $l_{max} = 2$ was taken. The number of reciprocal points for the SCF iterations was taken to be 10,648, which resulted in 834 points in the irreducible section of the Brillouin zone. An energy convergence within 0.01 mRy was kept in the relativistic calculations. The LDA to the exchange-correlation potential [16] along with the BROYDEN2 method [17] was employed. To calculate the valence Compton profiles, we have summed up the direction-dependent spin-up and spin-down Compton line shapes. The contribution of the core Compton profile was taken from the available free atom data [18]. The final absolute Compton profiles (free atomic core + KKR valence) were computed along the [100], [110] and [111] directions.

2.2. FP-LAPW Calculations

In order to obtain the electronic structure of W using the FP-LAPW scheme, we have used the WIEN-2k code [19, 20]. In this formalism, we have also used local orbitals (lo) for the high lying semi-core states. This method is supposed to give accurate results, as no shape approximation is made for the potential or charge density. In the present work, the radius of the muffin-tin sphere R_{MT} was chosen to be 2.5 a. u. The generalized gradient approximation (GGA) and the LDA schemes of [21, 22] were followed. The convergence criterion was set to 0.01 mRy; this is considered sufficient owing to the use of lo and APWs. For band structure calculations, 20 vectors in the irreducible Brillouin zone [500 ($7 \times 7 \times 7$) points] together with $R_{MT}K_{max} = 7.0$ were used. The maximum radial expansion was set to 10.

2.3. LCAO Calculations

We have also calculated the electronic structure using a linear combination of atomic orbitals as embodied in the CRYSTAL-03 code [23 – 25]. In the absence of all electron basis sets, the calculations were performed in the framework of ab-initio pseudo-potential (PP) with HF scheme, the DFT with LDA and GGA,

Table 1. Exchange and correlation functionals used in the HF and DFT calculations.

Theory	Exchange	Correlation
PP-HF	Hartree-Fock [23 – 25]	Neglected
PP-DFT-LDA	Dirac-Slater [23 – 25]	Perdew-Zunger [26]
PP-DFT-GGA	Becke [27]	Perdew-Wang [22, 28]
PP-B3LYP	Becke [27]	Lee-Yang-Parr [29]
		Vosko-Wilk-Nusair [30]

and the hybridization of HF scheme to DFT (so called B3LYP) [23]. In the PP formalism, the electron Hamiltonian operator includes kinetic, Coulomb, exchange-correlation, and effective core pseudo-potential (ECP) operators. It is worth mentioning that in the HF calculations the exact exchange interaction between electrons is taken care of, while the correlation effects are neglected. In case of DFT calculations, both the exchange and the correlation effects are treated approximately within the LDA and GGA. The exchange and correlation potentials [22 – 30], which were used in the present calculations, are listed in Table 1. The basis sets of W were taken from [31]. The SCF calculations were performed at 328 **k**-points in the irreducible Brillouin zone.

All the theoretical directional profiles were normalized to 26.54 e$^-$, being the area of the free atom Compton profile in the momentum range $0 - 7$ a. u. [18].

3. Experimental

For the directional Compton measurements we have employed a 3.7 GBq (100 mCi) ^{241}Am Compton spectrometer [32, 33]. For each individual measurement, identical single crystals of W (diameter, 8 mm; thickness, 3 mm) along the three major symmetry orientation [100], [110], and [111] were held vertically in the scattering chamber. The γ-rays, scattered on a mean angle of $(165 \pm 1.5)°$, were analyzed with a high-purity Ge detector. The overall momentum resolution of the spectrometer was 0.55 a. u. Gaussian full width at half maximum (FWHM). In each measurement, about $10.3 \cdot 10^6$ counts under the Compton peak were accumulated in about 560 h of exposure time. The background was measured separately and then subtracted point by point from the above data, after scaling it to the counting time of the sample. Thereafter the measured profile was corrected for the effects of detector resolution, energy-dependent absorption in the sample, Compton cross-section, and multiple scattering following the approach of the Warwick group [34, 35].
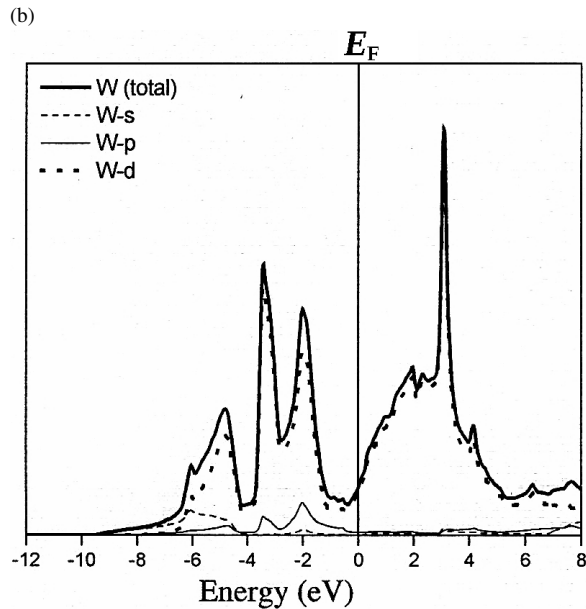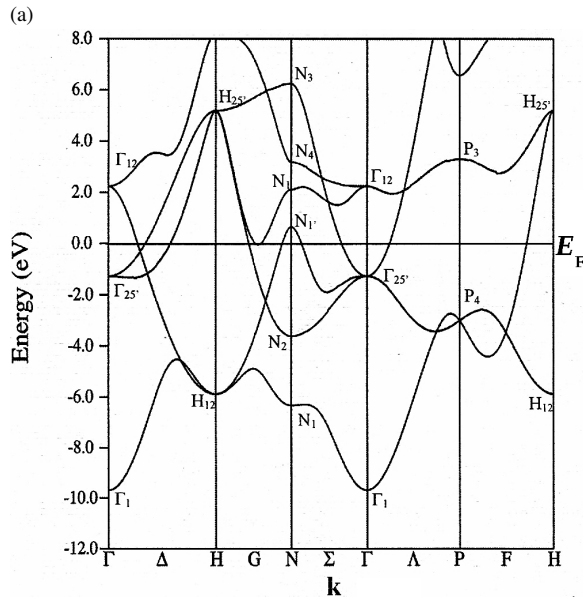
(a)

(a)

(b)

(b)

Fig. 1. (a) The electronic band structure of W along the high symmetry directions of the first Brillouin zone together with the total and the projected density of states (b) within the GGA approximation of FP-LAPW. The horizontal solid line corresponds to the Fermi energy (E_F).

Fig. 2. The same as in Fig. 1 for the LCAO (PP with DFT-GGA) scheme.

4. Results and Discussion

4.1. Energy Bands and Density of States

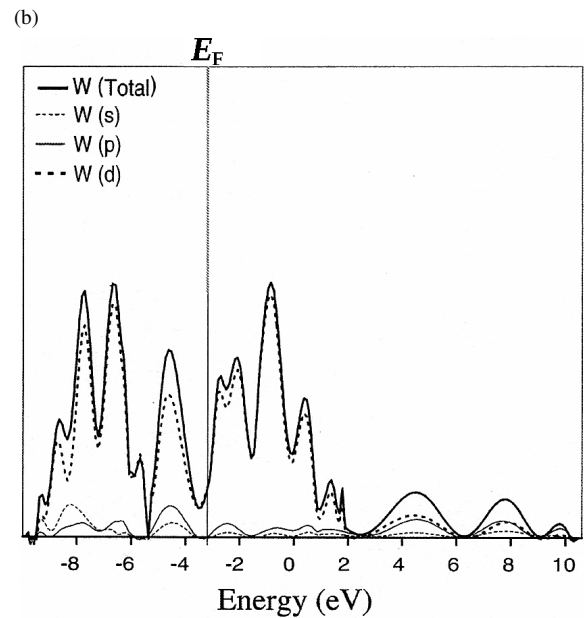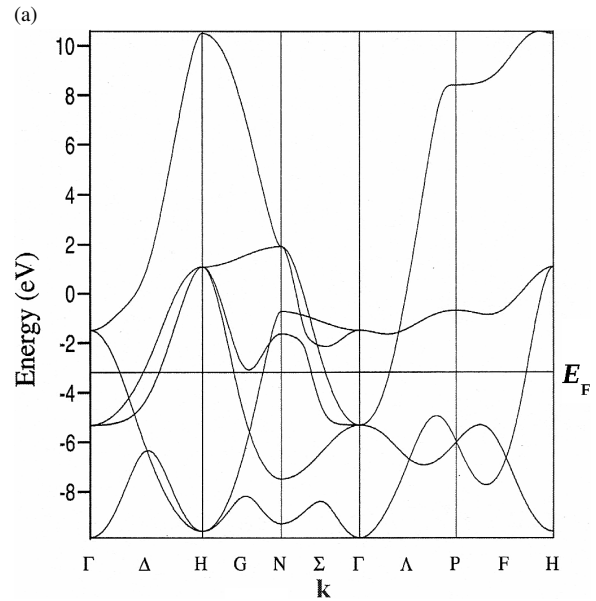The energy bands and the density of states, computed within the FP-LAPW, PP-DFT and SPR-KKR schemes, are shown in Figs. 1 – 3. Although the Fermi level consists of mixed 6s and 5d states, the energy bands show predominant 5d band states. In the bcc Bravais lattice, Γ, H and N are the important symmetry points in analyzing the energy bands. The state with Γ_1 symmetry represents the bottom of the 6s conduction band, while $N_{1'}$ represents a 6p-type state. At the symmetry points, the 5d-bands correspond to the Γ_{12}, $\Gamma_{25'}$,
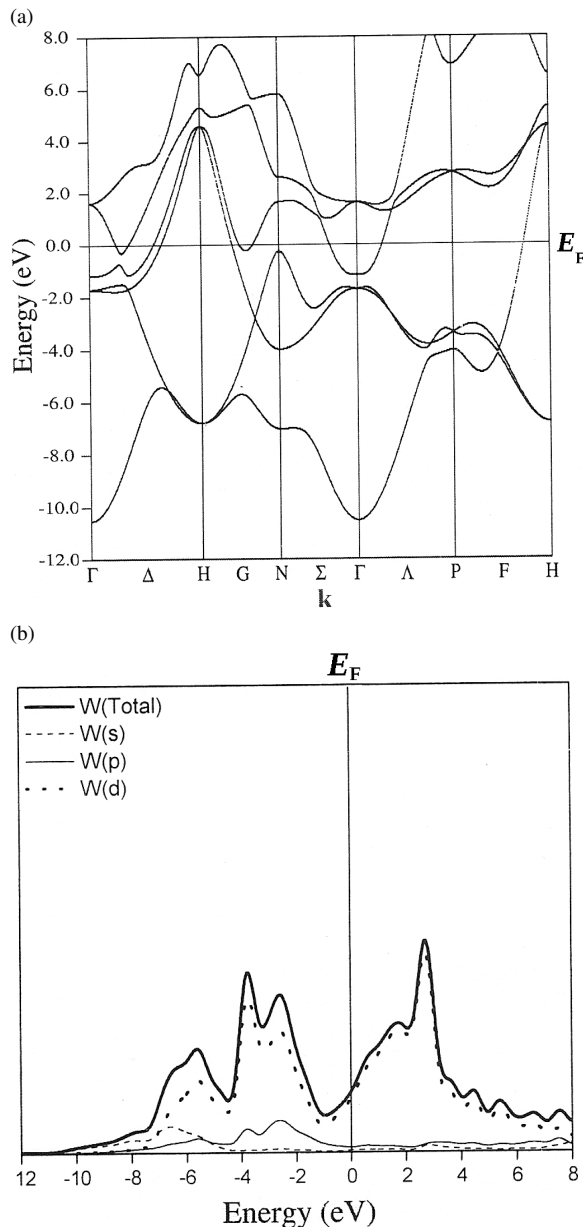
(a)

(b)

Fig. 3. The same as in Fig. 1 for the SPR-KKR scheme. The DOS is calculated for energies that have a constant imaginary part 0.01 Ry.

$H_{25'}$, H_{12}, N_3, N_4, N_1, N_2, $N_{1'}$, P_3, and P_4 states. In Figs. 1 and 2 a noteworthy feature in the band structure is the appearance of two small closed loops along the symmetry line from $\Gamma \to H$ (near H_{12}) and from $\Gamma \to P$. The shape of the small loop in the ΓH branch is not visible in Figure 3. It is due to the inclusion of the spin-orbit interaction in the SPR-KKR calculation.

In case of a semi-relativistic treatment (Figs. 1 and 2), this loop is derived from bands, which cross along the symmetry lines from Γ to H. On the other hand, in Γ-P direction a loop-like structure remains even after the inclusion of the spin-orbit corrections. It indicates that Γ-P is less affected by the inclusion of the spin-orbit interaction.

In Figs. 1 and 2 three bands cross the Fermi level along the line ΓH, one of which is doubly degenerated. In Fig. 3, the spin-orbit interaction in the SPR-KKR scheme lifts this degeneracy. It is seen that the 5d energy band at $\Gamma_{25'}$ shows splitting with two levels at -1.715 and -1.171 eV. Within the SPR-KKR approach, the 5d energy band at $H_{25'}$, also shows a similar splitting at 4.579 and 5.293 eV. In Figs. 1 and 2 the energy difference $\Delta d \equiv E(H_{25'}) - E(H_{12})$ is a measure of the d bandwidth. Our DFT-GGA, B3LYP, FP-LAPW (GGA) and FP-LAPW (LDA) calculations results in Δd values of 10.626, 11.486, 11.068, and 10.898 eV, respectively, while due to the relativistic nature of the SPR-KKR calculation Δd comes out to be 12.078 and 11.364 eV. The spin-orbit effect splits the P_4 bands to -4.062 and -3.382 eV. The s-d shift obtained from the $H_{12} - \Gamma_1$ energy difference comes out to be 3.742 and 3.795 eV, respectively, according to the SPR-KKR and FP-LAPW (GGA) calculations. However, the DFT-GGA (Fig. 2) and the present B3LYP calculations (not shown here) give a very narrow s-d shift, viz. 0.275 and 0.678 eV, respectively. An underestimation of the s-d shift may be due to some limitations of the pseudo-potential eigenfunctions. In Table 2 we compare few characteristic eigenvalues of the occupied energy bands calculated within the SPR-KKR, FP-LAPW, and PP-DFT schemes and the other available data [3, 5, 12] for the sake of comparison, all the computed and available eigenvalues corresponding to Γ_1 are taken to be zero.

The density of state (DOS) curves shown in the lower panel of Figs. 1–3 illustrate the contributions of the 6s, 6p, and 5d states to the total density. These curves along with the energy bandwidths of the valence bands confirm that the first two fully occupied bands have a mixed contribution of the 6s, 6p, and 5d states. The third band which crosses the Fermi level has contributions from the s and p states below the Fermi energy and a dominant contribution due to the d states above the Fermi level. The DOS curves reflect that the fourth band represents major contributions from the d states. The fifth band, which has small electron pockets, arises predominantly from the d state.

Table 2. Comparison of energy band eigenvalues (in eV) of W. All the eigenvalues have been shifted, so that the Γ_1 eigenvalues are the same.

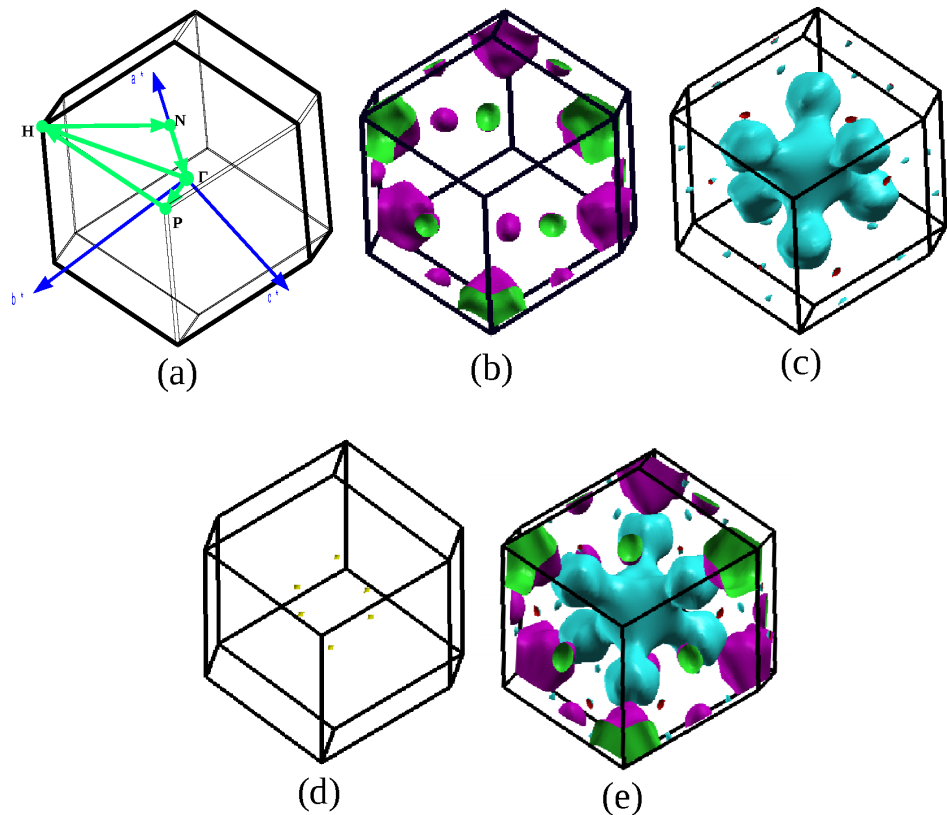| | BK | WKW | PBP | PP | | FP-LAPW | | SPR-KKR |
| | | | | | | — Present calculations — | | |
	[3]	[5]	[12]	B3LYP	DFT-GGA	LDA	GGA	LDA
Γ_1	0	0	0	0	0	0	0	0
$\Gamma_{25'}$	8.186	8.351	9.003	4.890	4.555	8.305	8.406	8.812, 9.356
Γ_{12}	11.611	11.825	12.081	10.275	8.362	11.731	11.918	12.146
N_1	3.252	3.295	3.655	0.767	0.580	3.333	3.353	3.504
N_2	5.871	5.994	6.647	2.520	2.387	6.016	6.068	6.533
$N_{1'}$	10.497	10.448	10.828	9.913	8.215	10.329	10.332	10.274
N_1	11.519	11.707	12.113	10.820	9.132	11.601	11.792	12.180
N_4	12.435	12.71	13.229	12.643	11.720	12.643	12.859	13.133
N_3	15.339	15.894	16.231	13.097	11.739	15.714	15.920	16.330
H_{12}	3.629	3.695	4.018	0.678	0.275	3.776	3.795	3.742
$H_{25'}$	14.412	14.852	15.217	12.164	10.901	14.674	14.863	15.106, 15.820
P_4	6.545	6.67	7.214	3.886	3.807	6.630	6.667	6.465, 7.145
P_3	12.589	12.87	13.254	11.064	9.173	12.749	12.977	13.269

Fig. 4. The Fermi surface of W using the FP-LAPW scheme. Shown here are: (a) the Brillouin zone for a bcc standard structure; (b) the third band hole octahedral around H points and small ellipsoidal closed hole pockets at the N points; (c) the fourth band electron jack centered at the Γ; (d) the fifth band small electron pockets (lenses) along the $\langle 100 \rangle$ directions; (e) an overall sketch (b+c+d) of Fermi surfaces.

4.2. Fermi Surface and Compton Profiles

The first Brillouin zone for the bcc structure is shown in Figure 4a. Figures 4b–d show the unique features of the individual band-based Fermi surface structures, deduced from the FP-LAPW-GGA calculations. Figure 4e illustrates the overall shape of the Fermi surface arising from all the valence states. It
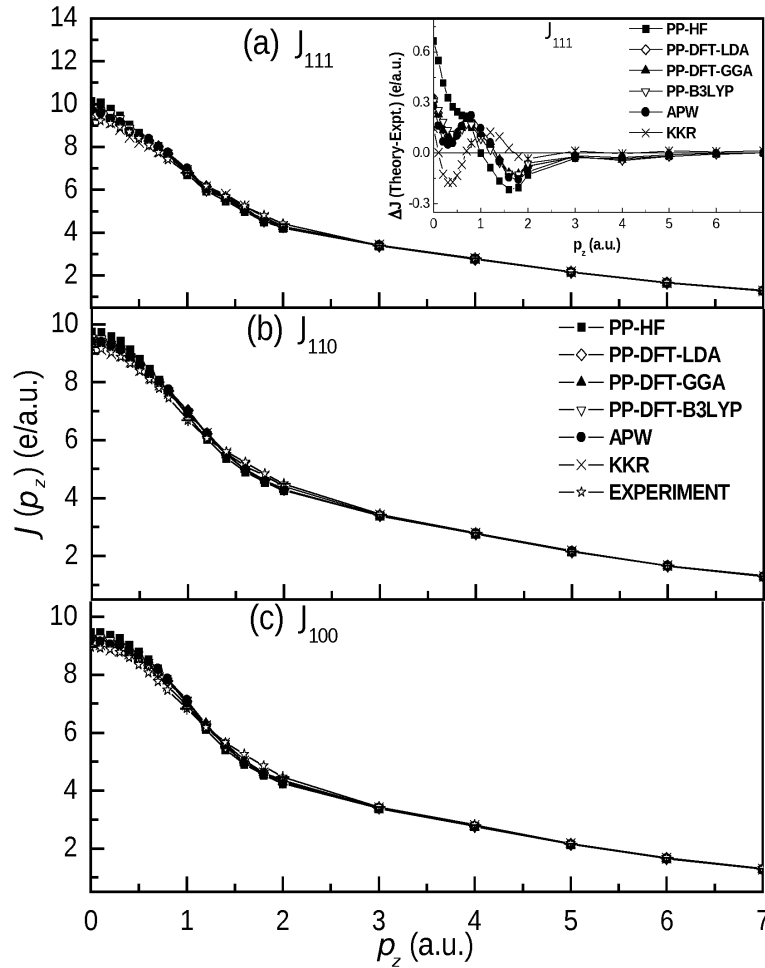
Fig. 5. The convoluted theoretical and experimental absolute Compton profiles of W for the (a) [111], (b) [110], and (c) [100] directions. The error is within the size of symbols. The inset shows the difference between the convoluted theoretical and experimental Compton profiles along the [111] direction.

is seen that at the origin (Γ point) of the Brillouin zone a closed octahedral body describes an electron 'jack'. The octahedral body is connected with six ball-like protrusions along the ΓH direction. Third band-based small hole pockets are visible at N. Since the directional Compton profiles are sensitive to the geometrical shape of the Fermi surface, the main features of the Fermi surface topology can also be understood in terms of the electron momentum densities. The present experimental and theoretical directional Compton profiles along with the semi-relativistic APW profiles [12] are presented in Figure 5. The theoretical profiles have been convoluted with the instrumental resolution of 0.55 a. u. (Gaussian FWHM). It is seen that the APW [12] and our DFT-GGA and B3LYP calculations exhibit almost similar behaviour. These theories overestimate the $J_{hkl}(p_z)$ in the low momentum range, $p_z < 1.0$ a. u., while a reverse trend is seen in the vicinity of $p_z = 2.0$ a. u. The PP-HF calculations show the poorest agreement with the experiment. For all directions, the SPR-KKR calculations show an overall better agreement with the experiment. The inset in Fig. 5a demonstrates a trend of agreement between the KKR theory and the experiment.

It is observed that the experimental values of $J_{100}(0)$, $J_{110}(0)$, and $J_{111}(0)$ are (8.963 ± 0.011), (9.225 ± 0.011), and (9.256 ± 0.011) e/a. u., respectively. $J_{111}(p_z)$ at $p_z = 0$ has the maximum value which implies that the overall momentum density is largest along the [111] direction. This behaviour can be understood by the fact that the projection of the momentum density $J_{111}(p_z)$ misses the hole Fermi surfaces at $p_z = 0$.
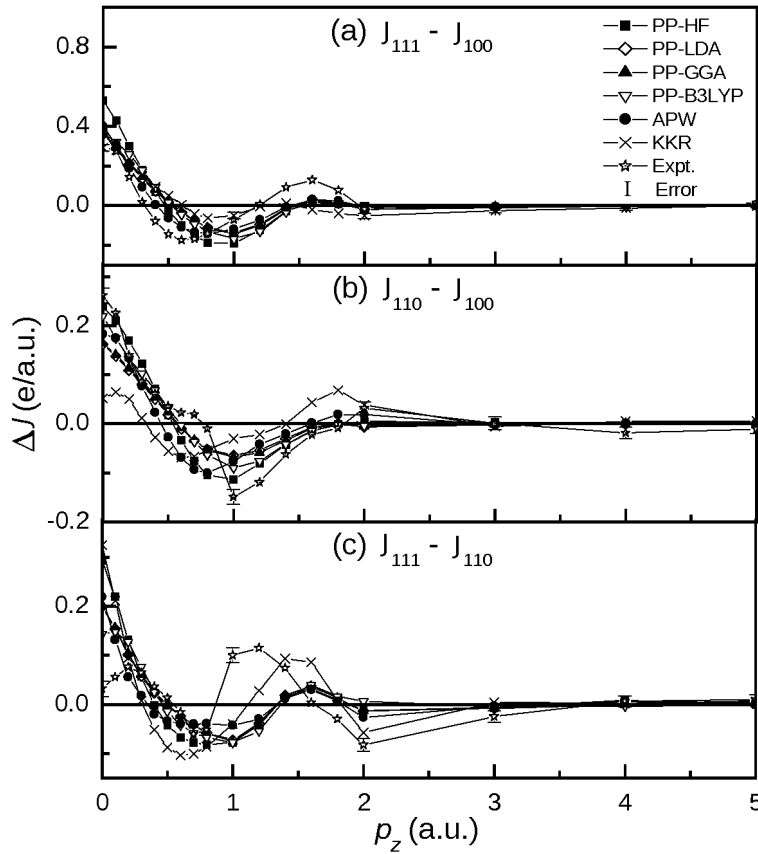
Fig. 6. Anisotropies (directional difference profiles) $\Delta J(p_z)$ for W for the following pairs of direction: (a) $J_{111} - J_{100}$, (b) $J_{110} - J_{100}$, and (c) $J_{111} - J_{110}$. All the theoretical profiles are convoluted with a Gaussian FWHM of 0.55 a. u. The APW data is taken from [12].

Since it is difficult to pick up any major structure in the absolute directional profiles, the data are analyzed via their anisotropic profiles as

$$\Delta J(p_z) = J_{h'k'l'}(p_z) - J_{hkl}(p_z). \tag{1}$$

The directional difference profiles exhibit characteristic oscillations, whose amplitudes are determined by details of the wave functions, while their pitch along the p_z-axis is coarsely determined by the fine structures of the momentum densities. Therefore, the anisotropy can be correlated to some specific features of the Fermi surface topology.

The theoretical and experimental directional difference profiles, $\Delta J(p_z)$, for the pair of directions $[111]-[100]$, $[110]-[100]$ and $[111]-[110]$ are presented in Figure 6. In most of the cases, the amplitudes of the oscillations in the anisotropies $\Delta J(p_z)$ are larger than in the experiment, being maximum in $[111]-[100]$. This supports the view that it is the $[111]$ occupation direction, which causes this discrepancy. This kind

of behaviour is attributed to the preferential occupation of triply (t_{2g}) degenerate orbitals, which are directed along the nearest [111] neighbour directions. The SPR-KKR calculations exhibit a fine structure in the anisotropy. In the low momentum region these calculations show larger anisotropy in the $[111]-[100]$ and $[111]-[110]$ directions, as compared to the $[110]-[100]$ directions. The fine structures in the SPR-KKR calculations may be due to the removal of degeneracy at few points of the Brillouin zone, which implies a redistribution of the electron density due to relativistic effects.

Now we interpret the periodicity in the anisotropic Compton profiles on the basis of the Fermi surfaces of W, consisting of hole or electron states. The overall shape of the Compton line is due to the first and second bands, which are filled. As can be seen from Fig. 4e, at the Γ point the plane of integration normal to the [100] direction will contain electron jacks at Γ and holes at N and H. At ΓH distances, the contribution of the occupied states is dominated by holes; there-

fore the momentum density will be small at $p_z = n \cdot \frac{2\pi}{a}$, where $n = 1, 2, 3 \ldots$. Furthermore, the plane of $[1\bar{1}0]$ scattering contains electron jacks at the point Γ and holes at N and H. This is also supported by the energy bands shown in Figs. 1–3. At the point Γ there are degenerate states near E_F at $\Gamma_{25'}$ and Γ_{12}, while at the N and H points such degeneracy is missing. In this case the holes and electrons contribute almost equally, so that there are no enhanced structures in the profile. Due to the disordered ellipsoidal holes centered at N, the momentum density corresponding to the ΓN distances ($0.745n$ a. u.) will give concave structures at these points. On the other hand, the plane for [111] scattering at $p_z = 0$ contains electron jacks at the Γ point and small hole pockets at N. The major contribution is from the jacks at Γ. Contribution due to a small hole-type structure at the ΓP ($0.910n$ a. u.) distances leads to shallow concavities.

The oscillations found in different anisotropies are consistent with the energy bands and the Fermi surface topology. In the case of anisotropies with respect to [100], $J_{111} - J_{100}$ and $J_{110} - J_{100}$, the positive amplitudes at $p_z = 0$ are due to concaves on J_{100} at ΓH distance ($n\frac{2\pi}{a} = 1.05n$ for W). Since the Γ electron jacks are extended towards the ΓH distances, J_{100} does not show a concave structure for $n = 1$. The crossover of anisotropies near $p_z = 0.5$ a. u. is due to the crossing of bands in the ΓH directions. The negative os-

cillation at about 0.7 a. u. in $J_{110} - J_{100}$ is due to the concave structure of J_{110} arising from ellipsoidal holes centered at N in the Σ branch. In the case of J_{111} the major contribution from the electron jacks at the Γ point gives a higher momentum density, which results in the largest value of J_{111} at $p_z = 0$ and is reflected in the anisotropies. Similarly, negative oscillations in $J_{111} - J_{110}$ near $p_z = 2.0$ a. u. are due to the small depressions of J_{111} near the ΓP distances.

5. Conclusions

We have discussed the electronic properties of W using the pseudo-potential, SPR-KKR, and FP-LAPW schemes. The first ever seen experimental anisotropies in Compton profiles are in a better agreement with the SPR-KKR theory. The anisotropy in the momentum density is discussed in terms of energy bands and Fermi surface topology. Synchrotron-based high resolution Compton measurements are required to reconfirm the applicability of the present SPR-KKR calculations in heavy transition metals like W.

[1] I. Petroff and C. R. Viswanathan, Phys. Rev. B **4**, 799 (1971).

[2] N. E. Christensen and B. Feuerbacher, Phys. Rev. B **10**, 2349 (1974).

[3] D. M. Bylander and L. Kleinman, Phys. Rev. B **27**, 3152 (1983).

[4] H. J. F. Jansen and A. J. Freeman, Phys. Rev. B **30**, 561 (1984).

[5] S. H. Wei, H. Krakauer, and M. Weinert, Phys. Rev. B **32**, 7792 (1985).

[6] G. J. Rozing, P. E. Mijnarends, and R. Benedek, Phys. Rev. B **43**, 6996 (1991).

[7] A. Debernardi, M. Alouani, and H. Dreysse, Phys. Rev. B **63**, 064305 (2001).

[8] M. J. G. Lee and Z. A. Ibrahim, Phys. Rev. B **70**, 125430 (2004).

[9] M. J. Cooper, Rep. Prog. Phys. **48**, 415 (1985).

[10] M. J. Cooper, P. E. Mijnarends, N. Shiotani, N. Sakai, and A. Bansil, X-Ray Compton Scattering, Oxford University Press, Oxford 2004.

[11] U. Mittal, B. K. Sharma, F. M. Mohammad, and B. L. Ahuja, Phys. Rev. B **38**, 12208 (1988).

[12] N. I. Papanicolaou, N. C. Bacalis, and D. A. Papaconstantopoulos, Handbook of Calculated Electron Momentum Distributions, Compton Profiles and X-Ray Form Factors of Elemental Solids, CRC Press, London 1991.

[13] H. Ebert, M. Battocletti, D. Benea, M. Kosuth, J. Minar, A. Perlov, and V. Popescu, The Munich SPR-KKR package, version 3.6; available from http://olymp.cup.uni-muenchen.de/ak/ebert/SPRKKR.

[14] H. Ebert, Fully Relativistic Band Structure Calculations for Magnetic Solids – Formalism and Application in Electronic Structure and Physical Properties of Solids (Ed. H. Dreysse), Lecture Notes in Physics, Springer, Berlin 2000, Vol. 535, p. 191.

[15] D. Benea, S. Mankovsky, and H. Ebert, Phys. Rev. B **73**, 094411 (2006).

[16] U. V. Barth and L. Hedin, J. Phys. C: Solid State Phys. **5**, 1629 (1972).

[17] D. D. Johnson, Phys. Rev. B **38**, 12807 (1988).

[18] F. Biggs, L. B. Mandelsohn, and J. B. Mann, At. Data Nucl. Data Tables **16**, 201 (1975).

[19] P. Blaha, K. Schwarz, and J. Luitz, WIEN Code, An

Augmented Plane Wave Plus Local Orbitals Program for Calculating Crystal Properties, Vienna University of Technology, Vienna, Austria 2001.

[20] P. Blaha, K. Schwarz, P. Sorantin, and S. B. Trickey, Comput. Phys. Commun. **59**, 399 (1990).

[21] J. P. Perdew, K. Burke, and M. Ernzerhof, Phys. Rev. Lett. **77**, 3865 (1996).

[22] J. P. Perdew and Y. Wang, Phys. Rev. B **45**, 13244 (1992).

[23] V. R. Saunders, R. Dovesi, C. Roetti, R. Orlando, C. M. Zicovich-Wilson, N. M. Harrison, K. Doll, B. Civalleri, I. J. Bush, Ph. D'Arco, and M. Llunell, CRYSTAL 2003 User's Manual, University of Torino, Torino 2003.

[24] C. Pisani and R. Dovesi, Int. J. Quantum Chem. **17**, 501 (1980).

[25] M. D. Towler, A. Zupan, and M. Causa, Comput. Phys. Commun. **98**, 181 (1996).

[26] J. P. Perdew and A. Zunger, Phys. Rev. B **23**, 5048 (1981).

[27] A. D. Becke, J. Chem. Phys. **98**, 5648 (1993).

[28] J. P. Perdew and Y. Wang, Phys. Rev. B **33**, 8800 (1986).

[29] C. Lee, W. Yang, and R. G. Parr, Phys. Rev. B **37**, 785 (1988).

[30] S. H. Vosko, L. Wilk, and M. Nusair, Can. J. Phys. **58**, 1200 (1980).

[31] Available from http://www.tcm.phy.cam.ac.uk/ mdt26/ basis_sets/W_basis.txt.

[32] B. L. Ahuja, V. Sharma, A. Rathor, A. R. Jani, and B. K. Sharma, Nucl. Instrum. Meth. B **262**, 391 (2007).

[33] B. L. Ahuja and N. L. Heda, Pramana-J. Phys. **68**, 843 (2007).

[34] D. N. Timms, Ph.D. Thesis, Compton Scattering Studies of Spin and Charge Momentum Densities, University of Warwick, England 1989.

[35] J. Felsteiner, P. Pattison, and M. J. Cooper, Phil. Mag. **30**, 537 (1974).